Influence of defect morphology and position on the fatigue limit of cast Al alloy: 3D characterization by X-ray microtomography of natural and artificial defects

Antonio Rotella, Yves Nadot, Mickaël Piellard, Rémi Augustin, Michel Fleuriot

Influence of defect morphology and position on the fatigue limit of cast Al alloy: 3D characterization by X-ray microtomography of natural and artificial defects

Antonio Rotella[a,b], Yves Nadot[a], Mickaël Piellard[b], Rémi Augustin[b], Michel Fleuriot[c]

[a]*Institut Pprime, CNRS, ISAE-ENSMA, Université de Poitiers, Téléport 2, 1 Avenue Clément Ader, 86961 Futuroscope Chasseneuil Cedex, France*

[b]*Safran Tech, Etablissement SAFRAN PARIS-SACLAY, 1 rue Geneviève Aubé, 78772, Magny Les Hameaux Cedex, France*

[c]*Centre Technique des Industries de la Fonderie, 44 Avenue de la Division Leclerc, 92310 Sèvres, France*

Abstract

The objective of the paper is to evaluate the impact of the morphology and the position of a casting defect on the fatigue limit of cast Al-Si alloy. Natural defects such as shrinkages reveal relatively complex morphology so the question is to understand the scale controlling the fatigue limit: the local one associated to inter dendritic porosity or the macroscopic one associated to the global geometry of the defect? In order to answer, fatigue tests are conducted on samples containing a spherical artificial defect of 700 µm. At the tip of the defect, three types of small defects aiming at representing inter-dendritic porosity are machined by EDM and FIB. Results show that there is no influence of a small defect at the tip of a big defect, meaning that the local morphology of the defect seems not to be the governing parameter. In addition, Finite Element simulations are conducted assuming that the global geometry of the defect could be described by an Equivalent Inertia Ellipsoid. Results show that this approximation of the defect gives good results for shrinkages. Finally, in order to understand the role of the position of the defect through the global volume of the sample, several samples have been analyzed through µCT before fatigue tests. Results are analyzed using Finite Element simulations taking into account for local cyclic plasticity and show that the defect can be considered as internal when the size of the shortest distance from the defect to the surface is bigger than the size of the defect.

Nomenclature

$(AREA)^{1/2}$	(μm)	Murakami's parameter defining the defect size
$(VOLUME)^{1/3}$	(μm)	Defect size parameter estimated by X-Ray microtomography
$\underline{\underline{X}}$	(MPa)	Hardening variable
$\underline{\underline{\varepsilon^p}}$	(-)	Plastic strain tensor
$\dot{p}$	(s^{-1})	Plastic strain rate
SDAS	(μm)	Secondary Dendrite Arms Spacing
σ_a	(MPa)	Stress amplitude
σ_D^{te}	(MPa)	Fatigue limit obtained with the "step by step" method with an uniaxial tensile test
E	(GPa)	Young's modulus
ν	(-)	Poisson's ratio
$R_{p0.2}$	(MPa)	Yield stress
R_m	(MPa)	Ultimate tensile strength
C	(MPa)	Material parameter in kinematic hardening model
γ	(-)	Material parameter in kinematic hardening model
$N_{failure}$	cycle	Number of cycles at failure of tested specimen in "step by step" method
N_{limit}	cycle	Number of cycles at which fatigue limit is estimated by "step by step" method
σ_n	(MPa)	Stress level at which specimen failed in "step by step" method
σ_{n-1}	(MPa)	Last stress level at which specimen did not fail in "step by step" method
$\bar{\bar{I}}_E$	($Kg{\cdot}m^2$)	Inertia tensor of a natural shrinkage
$\bar{\bar{I}}_S$	($Kg{\cdot}m^2$)	Inertia tensor of an equivalent ellipsoid
K_t^{pl}	(-)	Plastic stress concentration factor

1. Introduction

Cast materials are impacted by the presence of defects of different nature: shrinkages, gas pores, inclusions and oxides. A large number of such defects has an effect on the mechanical properties. A number of authors proved the detrimental effect of surface defects on fatigue strength of cast aluminum alloys [1–11]. The impact of a defect on fatigue strength can be characterized by its size, morphology and position. Buffière et al. [12] identified a relationship between the defect size and the sphericity of a defect, the authors found that gas pores are smaller and with a higher sphericity ratio compared to shrinkages. Several authors [7,10,13,14] performed studies by means of finite element simulations on the defect reconstructed after μ-CT scan. The main result indicates that the pore morphology influence the stress distribution. Li et al. [15] identified that the pore shape has an impact on the factor K_g (defined as the normalized stress/strain concentration factor). The authors determined that the stress distribution of a pore could be approximated using a sphere with the same projected surface on the transversal plane of the specimen. The difference over the evaluation of the K_g factor, between the real shape and the approximated shape, is 10%, showing that the complex morphology can be approximated by a

simpler shape, however the definition of the equivalent shape can modify the final result. Tijani et al. [16,17] proposed an empirical relation in order to simulate the fatigue life of cast aluminum alloys in presence of defects. The authors highlighted that a good correlation can be obtained if the effect of defect shape, size and position is taken into account. A recent study of Le et al. [7] proposed to take into account the effect of the defect morphology by testing two equivalent shapes (sphere and ellipsoid), their results show that the effect of the defect size is more pronounced for the complex shape defects compared to equivalent shapes in terms of Dang Van's criterion. The results show that the slope of the power trend line used to fit the real casting pores is higher than the slope of the trend line used for spherical pores. These results show that the effect of the size is more important for casting defects than spherical pores. A similar result has been obtained by Dezecot et al. [14], these authors pointed out via micro-tomography observations, that spherical pores are less detrimental than tortuous pores of the same size. The slope of the trend line used to fit the equivalent oblate ellipsoid is much closer to the one obtained for natural defects showing that a simplified geometry with a "sharper" morphology seems better to approximate the real casting morphology in terms of stress distribution.

A study conducted by Serrano-Munoz et al. [11] shows that the defect position plays an important role. The authors identified that crack growth rate is higher when a crack initiates and propagates from a surface defect (due to the environment), this effect is different when the crack initiates from an internal defect, since the propagation phase occurs probably under an inert environment close to vacuum. A very few studies [11,18–20] are addressing experimental fatigue crack propagation from internal defect but they mainly demonstrates that surface crack propagates much faster than internal ones.

From this analysis of literature results, it comes that the question of the morphology is important but none of the paper proposes a clear experimental protocol to demonstrate whether or not we should use the real 3D morphology or the equivalent global one. The first objective of this paper is to study the impact of local and global morphology of the defect on the fatigue limit. In addition to the morphology, position is also very important, a defect can be close to the surface, at the surface or internal. As it seems from the few experimental results available that surface defect are much more harmful than internal ones, it is very important to separate internal and surface defects when analyzing the criticism of defect in a component. This question will be addressed through the analysis of stress distribution computed around natural defects using Finite Element based on μCT scan of fatigue samples in order to propose a geometrical criterion to separate surface and internal defects. In order to consider only one family of defects, the analysis conducted in this work are mainly focused on shrinkages, porosities and artificial defects that simulates the shape of a cavity shrinkage (as defined by the ASTM standard [21]). Other defects such as oxides can be at the origin of the failure as shown in section 3.1 of this study. Therefore, during the experimental campaign, failure mainly occurred on "porosity type" defects, thus all the conclusions are based on the results and observations from this experimental database.

2. Materials and methods

2.1. Experimental procedures

2.1.1 Material

In this study, experimental fatigue tests have been carried out on an unmodified (without addition of Strontium) cast Al-Si-Mg alloy (A357) with a chemical composition reported in Table 1. The alloy didn't undergo any previous grain refinement operation. Concerning the casting process, a degassing procedure have been performed just before pouring the molten metal. This operation provides nitrogen bubbling by using a degassing rotor. Finally the alloy is poured at 710°C ± 5°C into a siliceous sand mould produced by using polyurethane process.

A T6 heat treatment has been performed before testing the specimens: (1) heating to solution 540°C for 10h; (2) quenching in cold water, (3) aging at room temperature for 24h; (4) aging at 160°C for 8h. A monotonic tensile test has been carried out to identify the mechanical static properties of the as received material (Table 2). The casting has been artificially degraded in order to introduce natural shrinkages. For this purpose, a customized casting mold has been used to cast the mechanical specimens. In order to obtain the casting shrinkage in the gauge section of the specimens, the cooling gradient has been artificially driven by using local chillers.

A previous study has been conducted using the same casting setup [22] developed at the CTIF (Centre Technique des Industries de la Fonderie) laboratory.

All the specimens have been subject to a finishing machining process leading to a good final surface quality (R_a=0.67 µm), the specimen size is given in Figure 1.

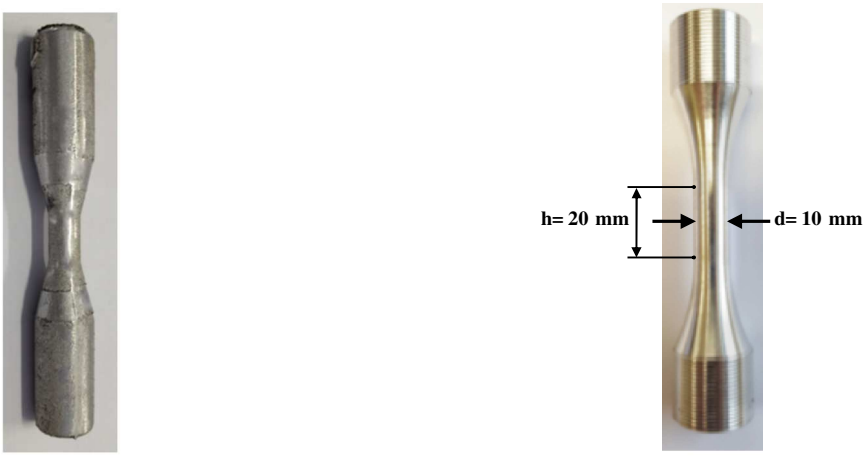

(a) **(b)**

Figure 1: Fatigue specimen, (a) As cast geometry, (b) machined sample.

Optical microscopy has been carried out (Figure 2) in order to estimate the Secondary Dendrite Arm Spacing (SDAS) that is of about 31 µm ± 8 µm. Grain size has also been measured after a Barker etching and the resulting size is of about 631 µm ± 46 µm. A columnar grain structure is observed near to the specimen surface (before machining), this is principally due to the contact between the molten metal and the mold. Therefore this zone is machined in order to extract the

fatigue specimen (diameter reduction from 13 mm to 10 mm) thus, the final tested granular microstructure is completely equiaxial.

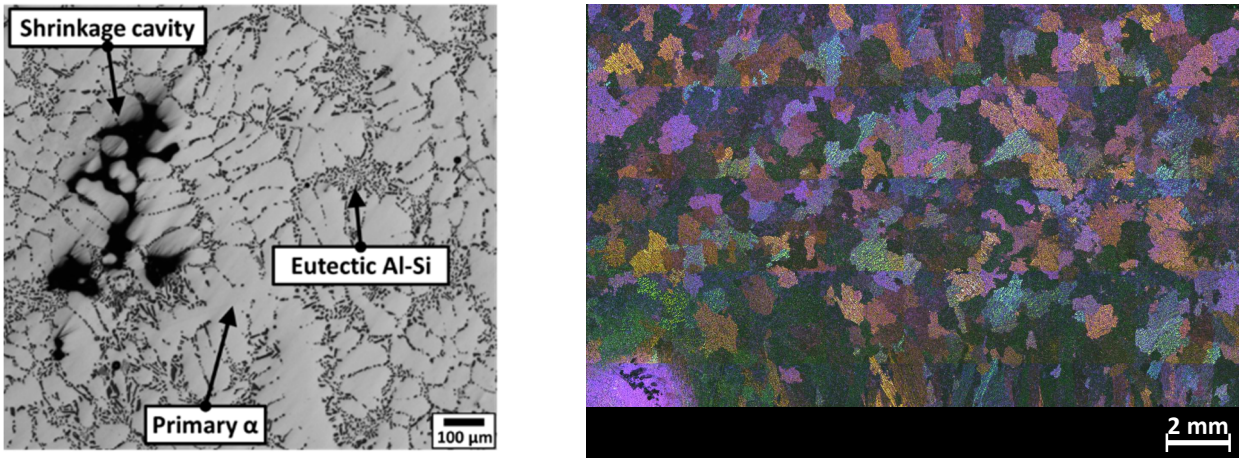

(a) **(b)**

Figure 2 : (a) A357-T6 microstructure, (b) A357-T6 microstructure after Barker etching (observed under polarized light).

Table 1 : Chemical composition of A357-aluminum alloy.

Si	Mg	Ti	Fe	Mn	Cu	Ni	Sn	Zn	Pb
7.05	0.57	0.16	0.12	<0.03	<0.015	<0.01	<0.01	<0.01	<0.003

Table 2 : Static tensile properties of the A357-T6 aluminum alloy.

E (GPa)	ν	$R_{p0.2}$ (MPa)	R_m (MPa)
73	0.3	275	335

2.1.2. Fatigue setup

All fatigue tests have been performed using a vibrophore Amsler 10 HFP 420 (electromagnetic resonance machine), providing a maximum load of 100 kN. The estimation of the fatigue limit has been conducted by using the "step by step method" [23,24]. The choice of this methodology has been justified by the need to obtain a fatigue limit for each sample. A standard fatigue testing using a staircase method [25] is not suitable because each specimen has a natural defect that is not repeatable in size, morphology and position, thus it is necessary to have a methodology that is capable to give an estimation of the fatigue limit for a given specific defect. The end of the test corresponds to a frequency drop of 1 Hz, which corresponds to a fatigue crack depth of 3 mm (the specimen gauge section diameter is equal to 10 mm). In order to estimate the fatigue limit, the first step is to test the specimen for a given stress σ, if the specimen does not fail and reaches the fixed number of cycles (for the current study $N_{limit} = 2 \cdot 10^6$ cycles) the fatigue test is started again on the same specimen by increasing the stress of an arbitrary Δσ. The procedure is repeated until the detection of a frequency drop of 1 Hz, which defines the end of the test (the failure stress is defined as σ_n). Finally, the fatigue limit is calculated using the Lanning proposition [24] that is

shown in equation 1. If the specimen fails at the first step (before reaching the value of N_{limit}), the fatigue limit can be estimated using a Basquin's law (equation 2), if it is possible to estimate the exponent m for the known loading condition.

$$\sigma_D = \frac{N_{failure}}{N_{limit}} \cdot (\sigma_n - \sigma_{n-1}) + \sigma_{n-1} \quad (1)$$

$$\sigma_D = C \cdot N^m \quad (2)$$

In the context of this study, the selected value of Δσ is 10 MPa. The application of the step by step method implies that the material is less, or not, sensitive to load history (no influence on the fatigue limit). For a cast aluminum alloy (A356-T6), very similar to the one of this study, any effect of the load history has been identified for different type of loads [3]. The same result has been obtained for others alloys such as titanium alloys [26] or 1045 steel [27]. Nevertheless, it is important to notice that a small crack can start to grow at the end of a step even if it is not long enough to activate a frequency drop of 1 Hz.

2.1.3. Artificial defect: EDM and FIB

To study the effect of defect morphology, the following procedure is proposed in order to have a controlled geometry at the macroscopic level (the big defect) and also at the local level representing inter-dendritic porosity (the local small defect). Artificial macroscopic surface spherical defect has been introduced using the EDM (Electron Discharge Machining) technique and the local defect morphology has been modified introducing a smaller defect (about 10 times smaller in diameter) at the tip of the spherical defect using a FIB (Focused Ion Beam) machining. The study is focused on the local defect morphology, for this purpose the macroscopic defect is a 1 mm diameter, spherical defect, introduced by EDM (a SEM image of the principal defect is given in Figure 3). Subsequently the local defect morphology have been modified introducing another smaller defect at the spherical defect tip.

Three local configurations have been studied:

1. Local 100 μm diameter defect obtained by EDM
2. Local 100 μm diameter defect obtained by FIB
3. Three local artificial cracks (half-disc shaped) obtained by FIB with a diameter of about 60 μm and a minimal distance between the defects of about 38 μm.

The choice of a distance of 38 μm between the crack shaped defects is correlated to the microstructure of the material and principally to the SDAS (31 μm ± 8 μm).

Figure 4 shows a SEM fractography of the specimens after failure with the three different local defect morphologies.

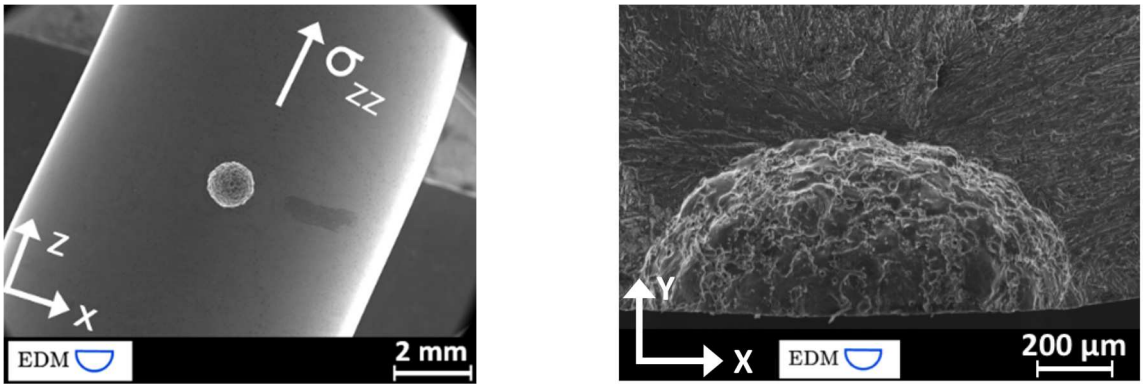

(a) (b)

Figure 3: (a) EDM 700 µm defect observed by SEM at the surface of the fatigue sample, (b) SEM observation of the fracture surface, initiation from the EDM 700 µm defect.

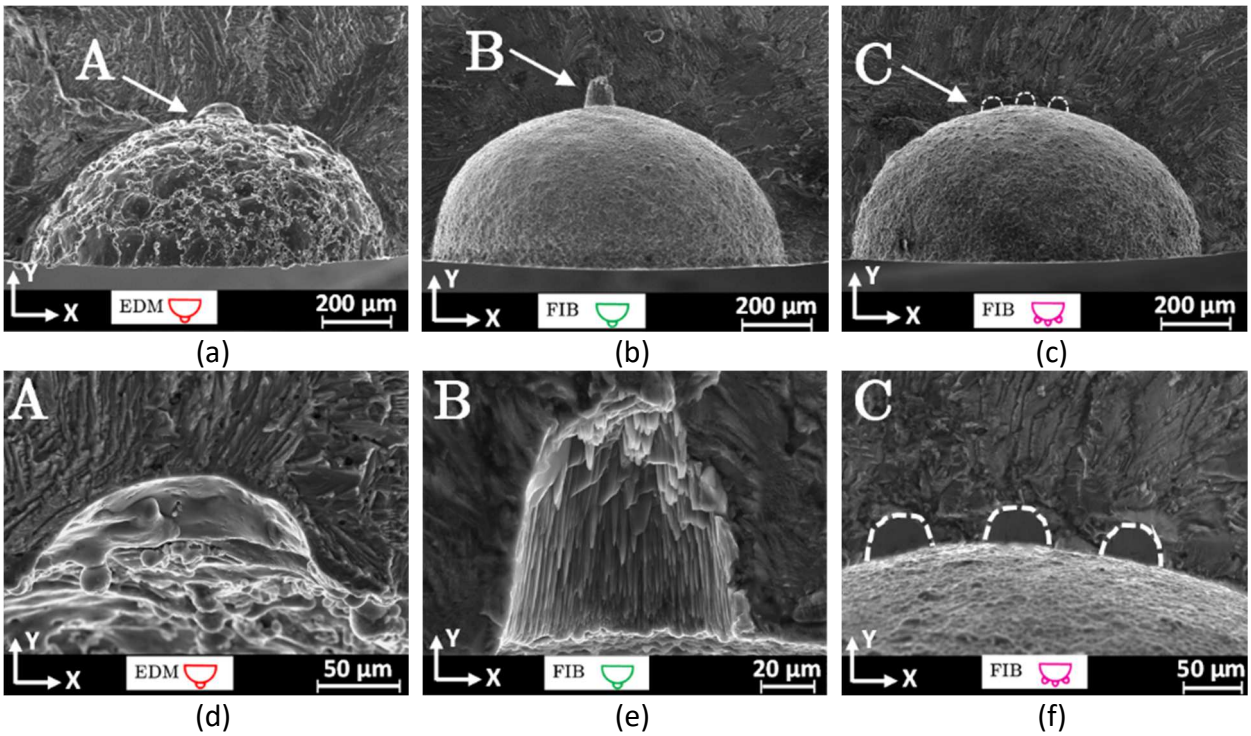

(a) (b) (c)

(d) (e) (f)

Figure 4: SEM observation of fracture surfaces, (a,d) small EDM defect at the tip of the 700 µm EDM defect, (b,e) small FIB spherical like defect at the tip of the 700 µm EDM defect, (c,f) 3 FIB crack like defect at the tip of the 700 µm EDM defect.

2.2. Numerical methods

The effect of defect morphology and position has also been analyzed by using FE (Finite Elements) simulations. The real casting defect morphology has been reconstructed after a μ-CT scan performed using a 150kV source giving a final voxel size of about 7μm. The 3D tomographic images have been processed in order to obtain the complete meshing of the outer surface of the defect and the surrounding Aluminum matrix. This methodology has been proposed by Dezecot et al. [14].

1. Grey level threshold of the images in order to obtain a binary 3D image (so called Volume A that also includes the air around the sample).
2. Extraction of the outer region to form the Volume B that fits closely the entire outer surface of the specimen. Pores can then be extracted (Volume C) by a boolean operation between volumes A and B.
3. Generation of two 3D surface meshes (linear triangles) using Avizo® commercial software corresponding to the internal pores surfaces from (Volume C) and the external shape of the sample (Volume B).
4. Surfaces merging and volume filling with quadratic tetrahedrons using the Gmsh software [28]
5. Reduction of the number of elements by 3D remeshing of the mesh generated at step 4. The size of the elements which are away from the sample and the pores surfaces are increased using the “distance plugin” of Gmsh to limit the number of degrees of freedom.

In order to obtain an accurate description of the stress/strain evolution a sensitivity analysis of the mesh size of the defect surface has been performed. This analysis have been conducted by examining the local response into a sub volume (cube shaped volume with a 2 mm side – Figure 5a) including a single defect issued from a specimen observed by μ-CT. The cube is loaded using a uniaxial tensile stress. The 3D element size around the defect is gradually increased starting from the defect surface (finer mesh) until the outer sub volume face (element size of 50 μm). The model response is evaluated by observing the evolution of the stress along the loading direction (S_{zz}). The stress evolution (Figure 5c) is observed along the AB path (Figure 5b) starting from the defect surface (A point) until the outer cube face (B point).

Three different mesh sizes of the defect outer surface have been tested (6μm, 9μm and 13μm), the result of the sensibility analysis is showed in Figure 5c. A similar result has been obtained with the three tested mesh sizes. The final choice has been to use the intermediate mesh size of 9μm in order to have more integration points locally around the defect and better describe the stress/strain distribution.

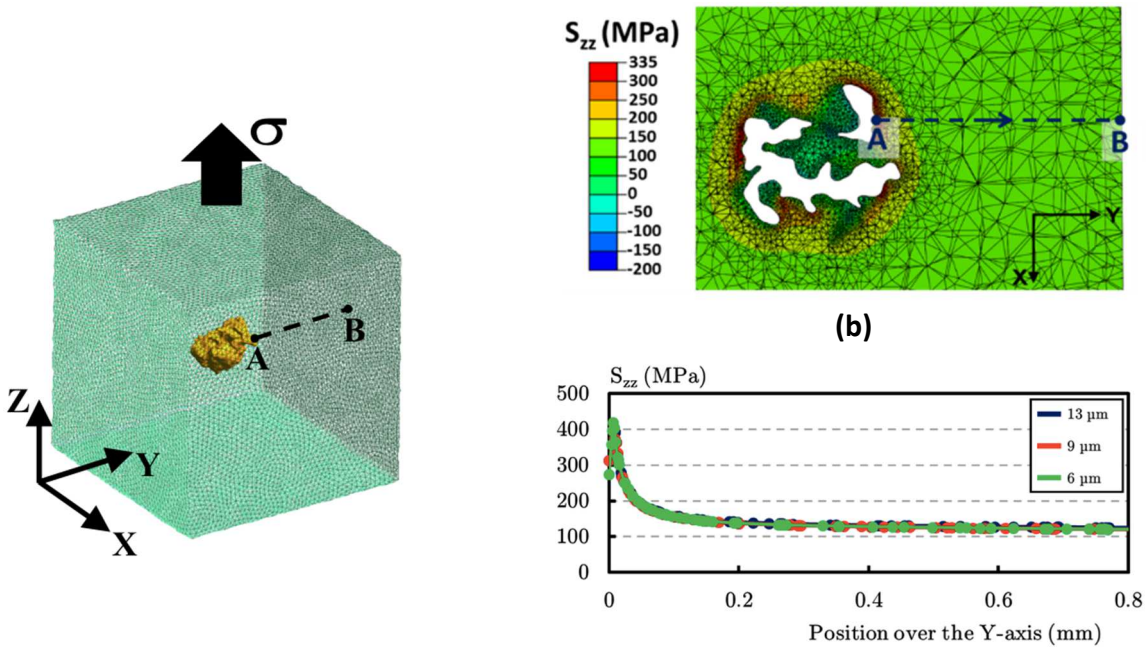

Figure 5: (a) surface mesh view of the cube model, (b) illustration of σ_{zz} result with the local mesh, (c) σ_{zz} distribution from point A with different mesh size.

2.2.1 Elastic-plastic material behavior law

The FE simulations are conducted considering the pores extracted from the specimens after observations by means of a µ-CT scan. The purpose of the FE simulations is to compute local stresses around a complex shaped defect. The FE model, as presented in section 2.2, is composed by an Aluminum alloy matrix (the material is considered isotropic without taking into account the local effect of eutectic and silicon particles). In order to model the aluminum matrix, a strain driven cyclic hardening test has been conducted. The stress/strain loops are shown in Figure 6. It can be pointed out that the material behavior can be principally described using a non-linear kinematic hardening law. In order to simplify the calculation the isotropic hardening has been considered negligible, thus a material's law based on the Lemaitre and Chaboche [29] model has been identified (equation 3).

$$\dot{\underline{X}} = \frac{2}{3} C \cdot \dot{\underline{\varepsilon}}^{p} - \gamma \cdot \underline{X} \cdot \dot{p} \qquad (3)$$

$\underline{X}$ is the hardening variable, $\underline{\varepsilon}^{p}$ is the plastic strain tensor, C and γ are material parameters, and $\dot{p}$ is the cumulated plastic strain rate.

Material parameters (C et γ) have been obtained on a stabilized stress/strain loop obtained for the 4 total strain levels, their value is given in Table 3.

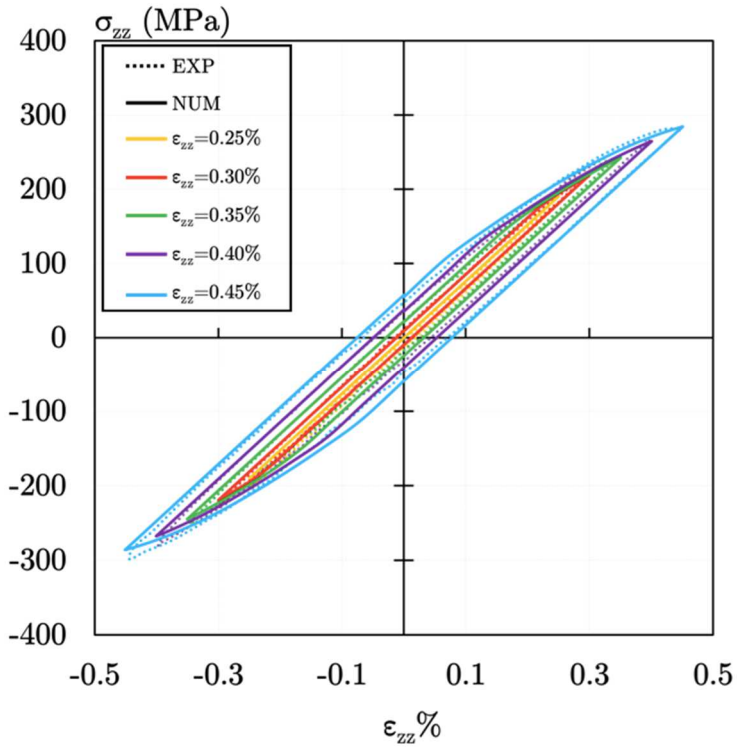

Figure 6: Experimental stabilized stress strain loop and comparison with numerical simulations to validate material parameters.

Table 3 : Kinematic hardening material parameters identified for the A357-T6 aluminum alloy.

C (MPa)	γ
150000	1400

The correlation between the experimental stress/strain loops (at the stabilized cycle) are compared with a numerical simulation result using the Lemaitre and Chaboche model of equation 3, results are shown in Figure 6. A good agreement between experimental test and numerical simulations is obtained, thus the model is retained for the FE element simulations of the stress field around a complex shaped defect.

2.2.2 FE simulations

The FE simulations have been conducted by considering the same loading conditions used during the fatigue test and a stress ratio R=0.1. In order to reduce the calculation time, the FE simulations have been conducted during 10 loading cycles. A stress analysis at each load cycle has been conducted and it has been observed that the stress behavior starts to be stabilized without any other modification of the mean stress, starting from the 10^{th} loading cycle. Only the gauge section of the specimen has been modeled using the same meshing criteria presented in section 2.2.

3. Results

Results are presented into two sections. The first one addresses only experimental results by the means of fatigue tests and SEM observations. The second section uses Finite Element modelling in order to evaluate the influence of the global morphology and the position of the defect on the fatigue limit.

3.1. Experimental results

This section describes the fatigue test results obtained on specimens with artificial defects as described in section 2.1.3.

Figure 7 shows the S-N fatigue diagram. All the fatigue specimens have been inspected by using X-Ray nondestructive control following the ASTM E2411 [21] before testing. In order to take into account only the artificial defect influence, the tested specimen are issued from the same ASTM class, that has been considered as the reference material (ASTM shrinkage grade < 1) [22].

Reference fatigue results (without artificial defects) are given by the black dashed line (Figure 7). The specimens have been tested using the step by step method presented in section 2.1.2. The global result shows that the introduction of an artificial defect introduces a fatigue strength reduction of about 25%. This effect is principally related to the principal spherical defect which size (expressed as $AREA^{1/2}$) is of about 700µm. A summary of the estimated fatigue limits is given in Table 4. The local “spherical” EDM defect (Figure 4d) as well as the FIB one (Figure 4e) lead to the same fatigue limit than the big defect without local modification. It seems therefore that a local defect representing inter-dendritic porosity does not influence the fatigue limit. Furthermore, if we machine 3 crack like FIB defects at the tip of the big defect, there is still no impact on the fatigue limit. These results lead to the conclusion that the local morphology is not the major parameter compared to the global one. This result is important because it suggests that we should focus on the “macroscopic” representation of the defect rather than the real local one when trying to assess the fatigue limit of cast Al-Si alloy.

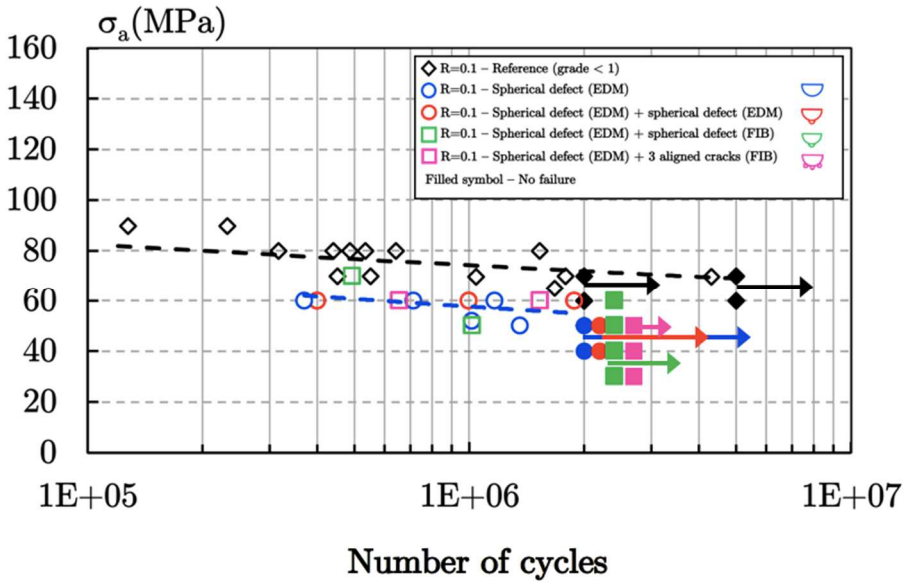

Figure 7: Fatigue test results obtained under tension at R = 0.1.

Table 4: Fatigue limit (at N=2·10^6 cycles) for each defect type.

Defect family	R	$\sigma^{ta}_{D\ 0.1}$ (MPa)
Reference (grade < 1)	0.1	69
Spherical defect (EDM)	0.1	52
Spherical defect (EDM) + spherical defect (EDM)	0.1	53
Spherical defect (EDM) + spherical defect (FIB)	0.1	54
Spherical defect (EDM) + 3 aligned cracks (FIB)	0.1	55

During the fatigue test performed on some artificial defect specimens, the critical failure of the specimen did not occur on the artificial defect but it has been induced by the presence of a natural defect. Figure 8 shows an example of a SEM fracture surface analysis conducted on two specimens that failed because of an oxide film (Figure 8a – specimen 25-4) or a natural cavity shrinkage (Figure 8b – specimen 28-1).

A deeper SEM analysis (Figure 8) has been conducted on the specimens showing this behavior (failure on a natural defect). A fatigue crack has been observed (for specimen 25-4) at the artificial defect tip indicating that, even though the initiation was longer than the critical natural defect, it still occurred. Therefore, the criticality of both defects can be considered very similar because they were both able to initiate a fatigue crack. It is important to notice that all the tested specimens have been checked by SEM at the tip of the big EDM defect before testing. The EDM and FIB machining didn't induce any local microcrack at the defect tip. It has been observed that the natural defect induces the specimen failure even if the size is lower than the artificial one (460µm for the oxide film; Figure 8a and 588 µm for the natural shrinkage – Figure 8b). This observation could be in contradiction with the first conclusion saying that the global morphology is much more important that the local one. Nevertheless, we can compare directly the regular sphere (EDM big defect) and the complex natural defect (588µm shrinkage) because the latest can't be considered

equivalent to a sphere. Thus, it is necessary to represent the global geometry of the defect through an equivalent quantity.

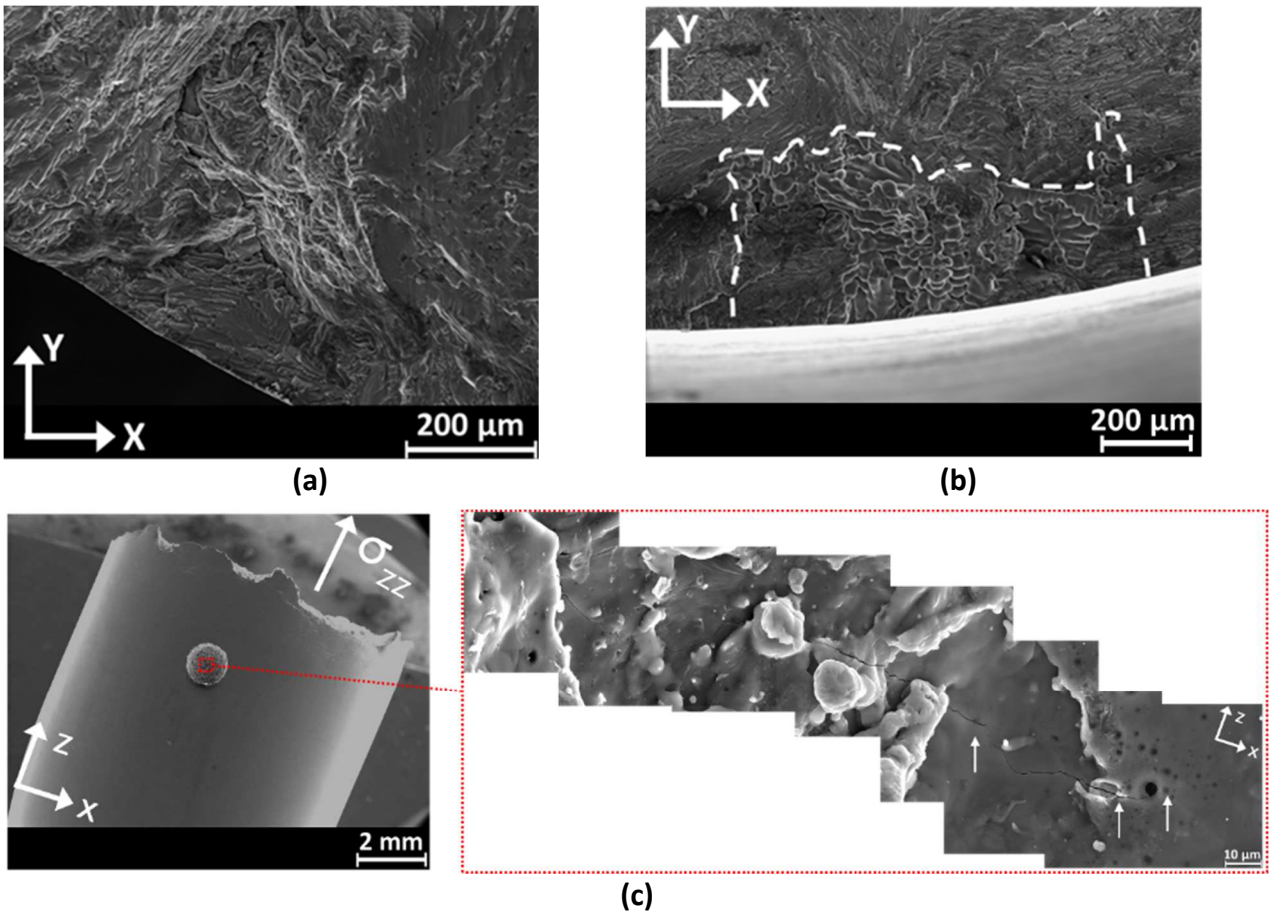

Figure 8: (a) crack initiation site of specimen 25-4 (ASTM grade <1), uniaxial tensile loading, R=0.1, σ_a = 60 MPa, N=9.96·10^5 cycles, with an artificial surface defect (AREA$^{1/2}$=700µm – see Figure 8c) - failure occurred onto an oxide film (AREA$^{1/2}$= 460µm), (b) crack initiation site of specimen 28-1 (ASTM grade <1), uniaxial tensile loading, R=0.1, σ_a = 60 MPa, N=1.53·10^6 cycles, with an artificial surface defect (AREA$^{1/2}$=654µm) - failure occurred onto an natural shrinkage (AREA$^{1/2}$=588µm), (c) internal view of the artificial surface defect of specimen 25-4 showing a small crack of about 200 µm.

3.2. FE simulations results

In order to perform complementary analysis of experimental results, FE simulations have been performed on the real shape of a natural defect. The simulation has been conducted by considering only the defect that leads to specimen's failure (observed on the fracture surfaces post-mortem). In order to evaluate the way to produce an equivalent geometry of a complex defect, two equivalent shapes are tested:

- An Equivalent Sphere (ES)
- An Equivalent Inertia Ellipsoid (EIE)

The equivalent sphere (ES) is calculated as a sphere with the same global volume as the natural defect. The EIE orientation in the 3D space follows the same principal inertia axis of the natural defect. In order to calculate the EIE, a MatLab® script has been developed, the main steps of the calculation are summarized below.

The first step is to calculate the inertia matrix ($\bar{\bar{I}}_S$.) of the natural shrinkage from µ-CT images. This matrix can be diagonalized into a global coordinate system and simplified as shown by equation 4.

$$\bar{\bar{I}}_S = \begin{bmatrix} I_{S,1} & 0 & 0 \\ 0 & I_{S,2} & 0 \\ 0 & 0 & I_{S,3} \end{bmatrix} \quad (4)$$

The same conditions can be applied for a generical ellipsoid defined by equation 5.

$$\frac{x^2}{a^2}+\frac{y^2}{b^2}+\frac{z^2}{c^2} = 1 \quad (5)$$

Thus the global inertia matrix of the ellipsoid can be written by following equation 6.

$$\bar{\bar{I}}_E = \begin{bmatrix} \frac{m}{5}\left(b^2+c^2\right) & 0 & 0 \\ 0 & \frac{m}{5}\left(a^2+c^2\right) & 0 \\ 0 & 0 & \frac{m}{5}\left(a^2+b^2\right) \end{bmatrix} \quad (6)$$

Where m is the ellipsoid mass and a, b and c are the ellipsoid semi-axis.

Imposing the equality of each principal inertia axis (equation 4 and equation 6) it is possible to obtain the result of equation 7.

$$I_{S,1} = \frac{m}{5}\left(b^2+c^2\right)$$

$$I_{S,2} = \frac{m}{5}(a^2+c^2) \quad (7)$$

$$I_{S,3} = \frac{m}{5}\left(a^2+b^2\right)$$

In this particular case the equivalence is defined only by a geometrical point of view, the mass (m) is imposed equal to 1 for both ellipsoid and natural shrinkage. The value of the ellipsoids semi-axis (a,b and c) can be calculated by using the condition of the triangular inequality (equation 8).

$$I_{S,1}+ I_{S,2} \geq I_{S,3}$$

$$I_{S,2}+ I_{S,3} \geq I_{S,1} \quad (8)$$

$$I_{S,3}+ I_{S,1} \geq I_{S,2}$$

In order to have the same orientation in the 3D space the center of gravity is considered equal for both the shrinkage and the ellipsoid.

3.2.1 Study of defect morphology effect

Four different natural defects have been studied, two parameters are used to characterize defect size as a unique scalar: the first one is the VOLUME $^{1/3}$ that makes no other interpretation than the geometry and the second one is the one proposed by Murakami [30] that combine geometry and loading. The defect sphericity (this parameter is equal to 1 for a perfect sphere) has also been calculated and the results are given in Table 5. The EF model has been defined by considering a cylinder with the same size of the specimens gage section (10 mm diameter and 20 mm eight).

Table 5 : Size and distance to the free surface for 4 natural defects.

Specimen	Defect	Sphericity	Size – T (µm) (calculated as VOLUME$^{1/3}$)	Distance from free surface - D (µm)	T/D
30-4	1	0.39	248	15.6	15.90
30-4	2	0.33	263	15.6	16.86
30-4	3	0.12	1214	1256	0.97
30-1	4	0.32	340	53.7	6.33

In order to take into account the effect of the local stress distribution, a local stress concentration factor (K_t^{pl}) has been defined. This parameter is calculated as the ratio between the local stress (in the loading direction) and applied stress. The local stress is calculated as follows:

- For real defect geometry the estimation has been done in the zone identified after an SEM fractography, as the local crack initiation size.
- For equivalent geometries (ES and EIE) it has been supposed that the crack initiation will occur in the real maximal stressed zone. Thus, the K_t^{pl} is calculated as the ratio between the maximal stress and the applied stress.

The defects are situated at a different distance from the specimen's surface. In order to take into account only the effect of the defect morphology, a parameter T/D is calculated as the ratio between the defect size and the minimal distance between the defect and the outer specimen surface.

The results of the FE simulations are to be intended as a relative comparison between real defect morphology and equivalent defect. This result is obviously influenced by the choice of the model used for the material behavior and does not take into account the local effect of microstructure and Silicon particles. A diagram showing the evolution of the K_t^{pl} in function of the parameter T/D is given in Figure 9 for the three geometries. From this diagram we can't be so confident on the results of the defect close to the surface because this proximity of the surface could modify strongly the stress distribution. It can be pointed out from the other computations that the EIE seems to give a better estimation of the local K_t^{pl} with respect to the equivalent sphere. Therefore, it is possible to conclude that the EIE could be used as an equivalent representation of a natural defect. This representation is easy to compute from µCT images and its main advantage is the possibility to keep the "defect orientation over space". This main feature seems necessary on a complex component when the geometry and the loadings leads to multiaxial local loadings. The ES can be used as a first order estimation but results will be less accurate compared to the EIE.

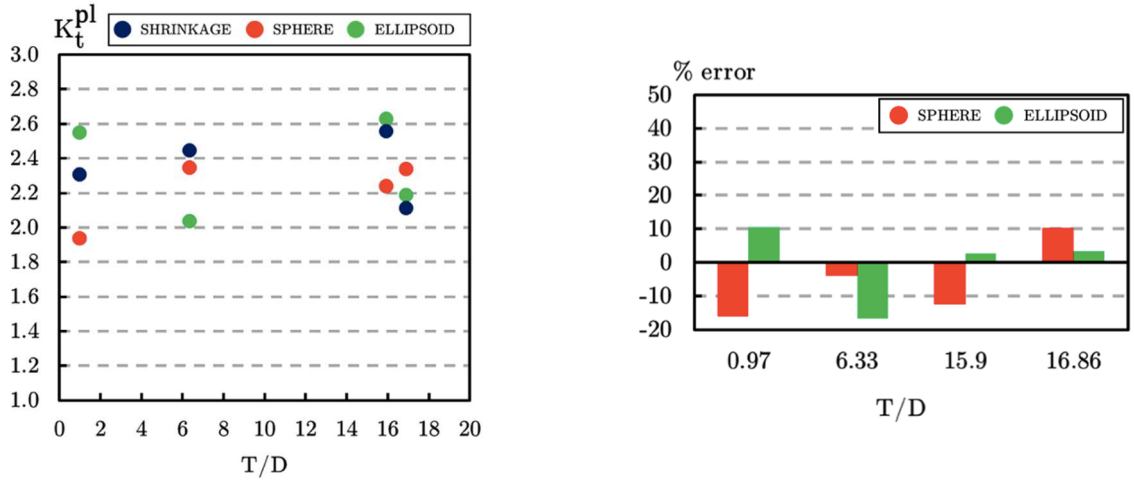

(a) **(b)**

Figure 9: (a) local value at the highest stressed point as a function of the distance of the defect to the free surface, (b) comparison between the 3D natural model and the approximation to a sphere or to the equivalent inertia ellipsoid.

3.2.2. Study of defect position effect

As previously proposed, the morphology of a real 3D natural defect can be idealized by an Equivalent Inertia Ellipsoid with fairly good results as regard to the local stress distribution. However different studies show that the defect position can be also an important parameter influencing the fatigue life of metallic materials [10,18,19,31]. Serrano Munoz et. Al [11], for example, demonstrated that the fatigue crack propagation ratio is completely different when fatigue crack occurs onto a surface or an internal defect (more or less 10 times slower for internal defects). This effect is principally due to the external environment exposure of the crack. As proved in different previous studies, [1,3,11,22,27] the environment under which the defect initiates and propagates has a notable effect on the fatigue limit of the material that is almost not sensitive to the effect of defect size. Internal defect will lead to an internal crack that propagates under an inert environment (close to the vacuum) that slows fatigue crack propagation. The effect of the environment has been proved with experiments on specimens with surface defects under vacuum environment [10,11]. Crack propagation ratio are similar to internal defect crack propagation. Those two propagation mechanisms lead to different fracture surfaces (typical smooth fracture surface for surface defect – air environment) and pseudo-stage II fracture surfaces [32] for internal defect (under inert or vacuum environment).

The role of defect position with respect to the fatigue life assessment of cast component seems to be crucial. Up to now, no criteria to define if a defect should be considered as internal or surface defect is adopted during NDT (Non Destructive Testing). A correlation between experiments and FE simulations have been conducted in this section in order to propose a criteria to differentiate an internal from a surface defect and understand the behavior of a subsurface defect. By using µ-CT analysis, the real defect shape of a shrinkage defect has been reconstructed and meshed using the methodology described in section 3.1. The meshed defect correspond to a defect that leads to failure a specimen and induced a surface crack propagation (see example in Figure 10).

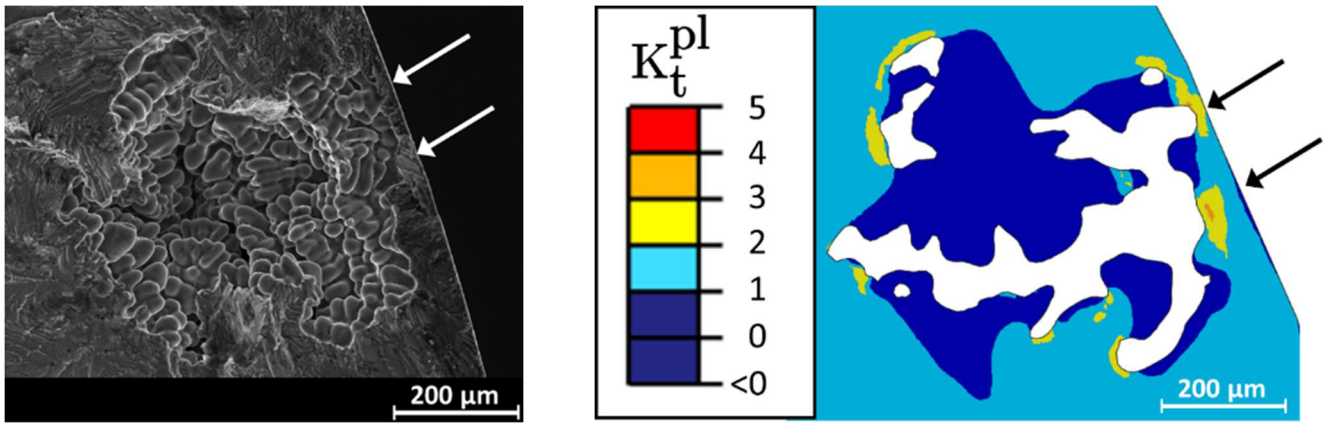

(a) **(b)**

Figure 10: (a) SEM view of the fracture surface, (b) result of the local stresses around the defect.

The defect characteristics (size, distance from surface and sphericity) corresponds to the defect 1 of Table 5.

In order to understand if the defect position can also influence the stress distribution around the defect, four defect positions from free surface have been meshed:

- Simulation 1: Real defect distance (15µm)
- Simulation 2: Distance = (defect size) / 2 = 124µm
- Simulation 3: Distance = defect size = 248µm
- Simulation 4: Distance = 2 · (defect size) = 496µm

The first simulation has been conducted by considering the defect in the real position (about 15µm from free surface). The other simulations have been conducted by considering a minimal distance from free surface that is related to defect size (expressed as VOLUME$^{1/3}$). As proposed in section 3.2.1 the evolution of the stress state around the defect has been evaluated by using a simple scalar parameter defined as K_t^{pl}. The parameter has been calculated in the crack initiation zone (observed post-mortem on fracture surfaces). In order to have a relative comparison, K_t^{pl} has been evaluated in the same zone also for the four FE simulations. The evolution of the K_t^{pl} in function of defect position (expressed as distance from free surface) is given in Figure 11c.

In order to be consistent with the previous section, we also compared the evolution of the K_t^{pl} when the real defect is represented by the sphere or by the equivalent inertia ellipsoid. Results are presented in Figure 11 for the three representations of the defect and for the four distances to the free surface.

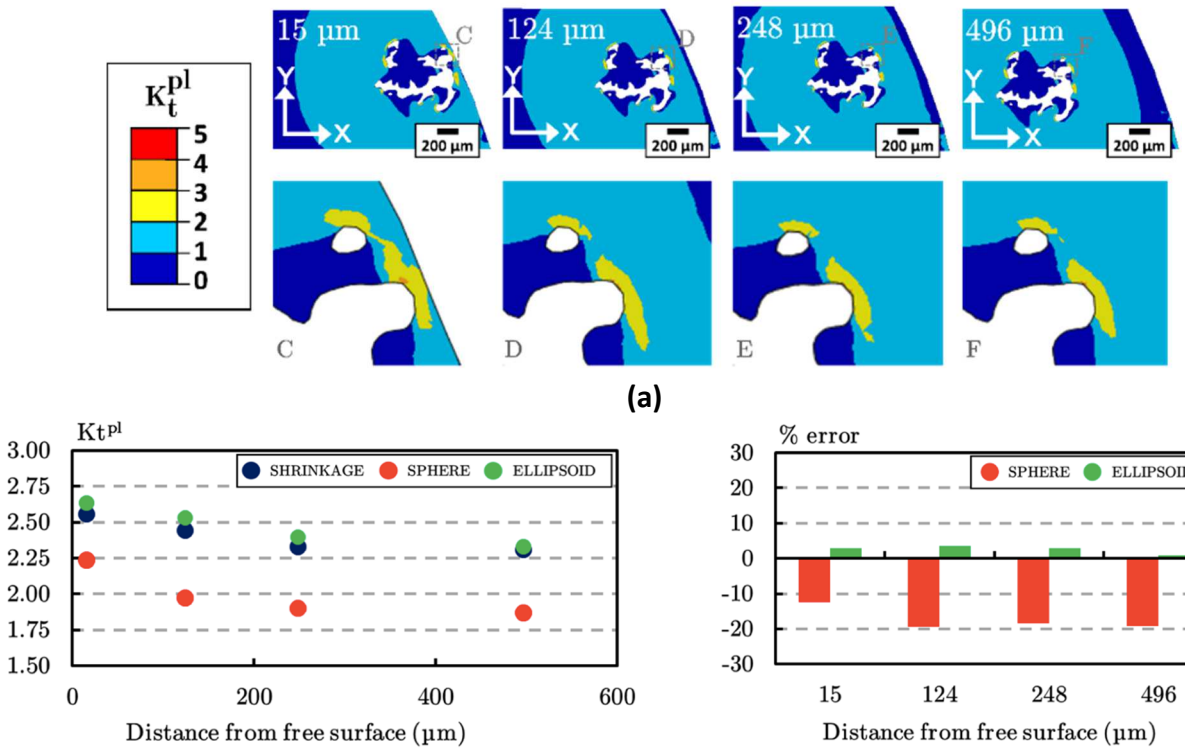

Figure 11: (a) comparison of local stresses around the defect when the distance to the free surface vary, (b) comparison between 3D model, sphere and ellipsoid as a function of distance to the surface, (c) comparison between the 3D natural model and the approximation to a sphere or to the equivalent inertia ellipsoid.

It can be pointed out that an evolution of the K_t^{pl} can be observed whatever the representation of the defect. The K_t^{pl} is higher for simulation 1, when defect is in its real position (15 µm from free surface). The value of the K_t^{pl} is decreasing when distance from free surface is increasing. However this effect seems to be less pronounced when the distance from free surface is at least equal to defect size (248 µm) and the K_t^{pl} value seem to saturate when the distance is higher than defect size (496 µm).

Therefore it seems reasonable to propose the following criterion:

A defect is considered to be internal when the size of the shortest distance to the free surface is bigger than the defect size measured using VOLUME$^{1/3}$.

In order to test the criterion on a consistent number of samples, a series of fatigue tests has been post-processed. The results are related to fatigue specimens tested into the HCF regime for a stress ratio R=0.1. Those specimens failed because of a surface, subsurface or internal defect and the two fatigue crack regimes described at the beginning of section 3.2.2 have been observed on the fracture surfaces. All specimens have been analyzed by µ-CT before testing and the defect leading to failure has been identified by correlating the SEM fracture surface analysis and the reconstructed µ-CT images.

A diagram correlating the defect size vs the distance from free surface has been plotted (see Figure 12). Defects that lead to a surface crack propagation are identified by red symbol, defects

that lead to an internal crack initiation are identified by a green symbol, other defects (not leading to a fatigue crack) are identified by a blue symbol. The frontier “defect size = defect position” is represented by a black dashed line. As shown by the diagram, the internal crack initiation always occurs on defects that are far enough from the external surface. Results agree with the proposed criterion, internal crack initiation occurs on defects with a position that is at least equal to the defect size (as proposed in the criterion).

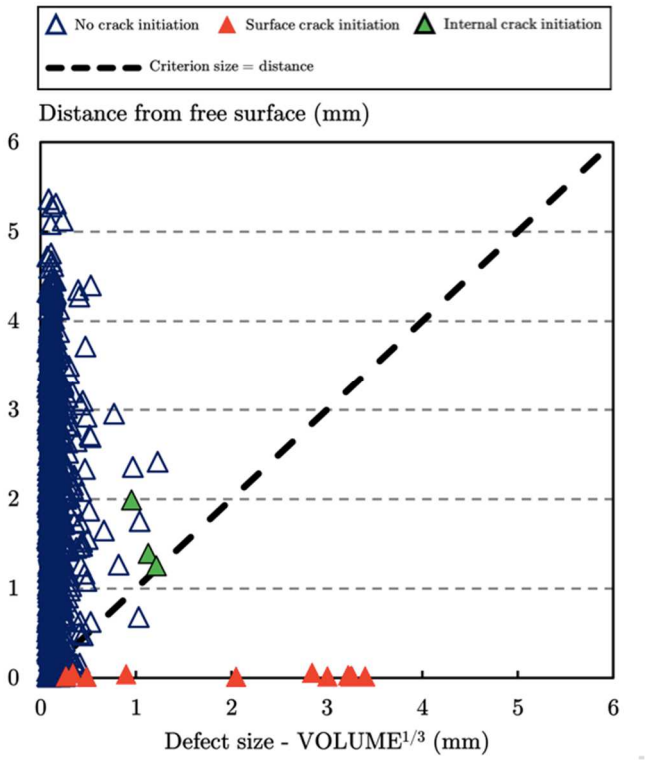

Figure 12: Validation of the definition of an internal crack.

4. Conclusions

Fatigue tests have been conducted in the High Cycle Fatigue range, under tension with a load ratio of 0.1 on a cast Al-Si alloy in order to evaluate the impact of position and morphology of defects on the fatigue limit. µCT scans have been performed on the fatigue samples before the test (voxel size: 7 µm) in order to be able to compute cyclic local stresses using a non-linear kinematic hardening plasticity model. Results obtained can be summarized as follows:

- The local morphology of a shrinkage, associated with interdendritic porosity, is not the major parameter influencing the fatigue limit.

- In order to find an equivalent geometrical representation of a real defect, three models are compared: the 3D real natural defect, an equivalent sphere with the same volume and an Equivalent Inertia Ellipsoid. From the viewpoint of local stresses, the Equivalent Inertia Ellipsoid is a better approximation of the defect than a sphere. Furthermore, this geometrical simplification allows to keep the main orientation of the defect over space, which is very important in a multiaxial context on real component.

- From the analysis of the stress distribution around a defect when the distance of the defect from the free surface changes, it can be concluded that a defect is considered to be internal when the size of the shortest distance to the free surface is bigger than the defect size measured using $VOLUME^{1/3}$.

5. Acknowledgment

Computations have been performed on the supercomputer facilities of the Mesocentre de calcul SPIN Poitou Charentes. This work was supported by the CPER FEDER project of Région Nouvelle Aquitaine. This work was partially funded by the French Government program “Investissements d'Avenir” (EQUIPEX GAP, reference ANR-11-EQPX-0018).

6 .References

[1] P. Mu, Y. Nadot, C. Nadot-Martin, A. Chabod, I. Serrano-Munoz, C. Verdu, Influence of casting defects on the fatigue behavior of cast aluminum AS7G06-T6, Int. J. Fatigue. 63 (2014) 97–109. https://doi.org/10.1016/j.ijfatigue.2014.01.011.

[2] P. Mu, Y. Nadot, I. Serrano-Munoz, A. Chabod, Multiaxial fatigue design of cast parts: Influence of complex defect on cast AS7G06-T6, Eng. Fract. Mech. 131 (2014) 315–328. https://doi.org/10.1016/j.engfracmech.2014.08.007.

[3] M. Iben Houria, Y. Nadot, R. Fathallah, M. Roy, D.M. Maijer, Influence of casting defect and SDAS on the multiaxial fatigue behaviour of A356-T6 alloy including mean stress effect, Int. J. Fatigue. 80 (2015) 90–102. https://doi.org/10.1016/j.ijfatigue.2015.05.012.

[4] M.J. Roy, Y. Nadot, D.M. Maijer, G. Benoit, Multiaxial fatigue behaviour of A356-T6, Fatigue Fract. Eng. Mater. Struct. 35 (2012) 1148–1159.

[5] M.J. Roy, Y. Nadot, C. Nadot-Martin, P.-G. Bardin, D.M. Maijer, Multiaxial Kitagawa analysis of A356-T6, Int. J. Fatigue. 33 (2011) 823–832. https://doi.org/10.1016/j.ijfatigue.2010.12.011.

[6] E. Pessard, D. Bellett, F. Morel, I. Koutiri, A mechanistic approach to the Kitagawa–Takahashi diagram using a multiaxial probabilistic framework, Eng. Fract. Mech. 109 (2013) 89–104. https://doi.org/10.1016/j.engfracmech.2013.06.001.

[7] V.-D. Le, N. Saintier, F. Morel, D. Bellett, P. Osmond, Investigation of the effect of porosity on the high cycle fatigue behaviour of cast Al-Si alloy by X-ray micro-tomography, Int. J. Fatigue. 106 (2018) 24–37. https://doi.org/10.1016/j.ijfatigue.2017.09.012.

[8] V.-D. Le, F. Morel, D. Bellett, N. Saintier, P. Osmond, Multiaxial high cycle fatigue damage mechanisms associated with the different microstructural heterogeneities of cast aluminium alloys, Mater. Sci. Eng. A. 649 (2016) 426–440. https://doi.org/10.1016/j.msea.2015.10.026.

[9] V.-D. Le, F. Morel, D. Bellett, N. Saintier, P. Osmond, Simulation of the Kitagawa-Takahashi diagram using a probabilistic approach for cast Al-Si alloys under different multiaxial loads, Int. J. Fatigue. 93, Part 1 (2016) 109–121. https://doi.org/10.1016/j.ijfatigue.2016.08.014.

[10] I. Serrano-Munoz, J.-Y. Buffiere, R. Mokso, C. Verdu, Y. Nadot, Location, location & size: defects close to surfaces dominate fatigue crack initiation, Sci. Rep. 7 (2017) 45239. https://doi.org/10.1038/srep45239.

[11] I. Serrano-Munoz, J.-Y. Buffiere, C. Verdu, Y. Gaillard, P. Mu, Y. Nadot, Influence of surface an internal casting defects on the fatigue behaviour of A357-T6 cast aluminium alloy, Int. J. Fatigue. (2015). https://doi.org/10.1016/j.ijfatigue.2015.07.032.

[12] J.-Y. Buffière, S. Savelli, P.-H. Jouneau, E. Maire, R. Fougeres, Experimental study of porosity and its relation to fatigue mechanisms of model Al–Si7–Mg0. 3 cast Al alloys, Mater. Sci. Eng. A. 316 (2001) 115–126.

[13] N. Vanderesse, E. Maire, A. Chabod, J.-Y. Buffière, Microtomographic study and finite element analysis of the porosity harmfulness in a cast aluminium alloy, Int. J. Fatigue. 33 (2011) 1514–1525.

https://doi.org/10.1016/j.ijfatigue.2011.06.010.

[14] S. Dezecot, V. Maurel, J.-Y. Buffiere, F. Szmytka, A. Koster, 3D characterization and modeling of low cycle fatigue damage mechanisms at high temperature in a cast aluminum alloy, Acta Mater. 123 (2017) 24–34. https://doi.org/10.1016/j.actamat.2016.10.028.

[15] P. Li, P.D. Lee, D.M. Maijer, T.C. Lindley, Quantification of the interaction within defect populations on fatigue behavior in an aluminum alloy, Acta Mater. 57 (2009) 3539–3548. https://doi.org/10.1016/j.actamat.2009.04.008.

[16] Y. Tijani, A. Heinrietz, T. Bruder, H. Hanselka, Quantitative evaluation of fatigue life of cast aluminum alloys by non-destructive testing and parameter model, Int. J. Fatigue. 57 (2013) 73–78. https://doi.org/10.1016/j.ijfatigue.2013.05.017.

[17] Y. Tijani, A. Heinrietz, W. Stets, P. Voigt, Detection and Influence of Shrinkage Pores and Nonmetallic Inclusions on Fatigue Life of Cast Aluminum Alloys, Metall. Mater. Trans. A. 44 (2013) 5408–5415. https://doi.org/10.1007/s11661-013-1773-0.

[18] T.P. Chapman, K.M. Kareh, M. Knop, T. Connolley, P.D. Lee, M.A. Azeem, D. Rugg, T.C. Lindley, D. Dye, Characterisation of short fatigue cracks in titanium alloy IMI 834 using X-ray microtomography, Acta Mater. 99 (2015) 49–62. https://doi.org/10.1016/j.actamat.2015.07.069.

[19] F. Yoshinaka, T. Nakamura, S. Nakayama, D. Shiozawa, Y. Nakai, K. Uesugi, Non-destructive observation of internal fatigue crack growth in Ti–6Al–4V by using synchrotron radiation μCT imaging, Int. J. Fatigue. 93 (2016) 397–405. https://doi.org/10.1016/j.ijfatigue.2016.05.028.

[20] A. Messager, A. Junet, T. Palin-Luc, J. Buffiere, N. Saintier, N. Ranc, M. El May, Y. Gaillard, A. King, A. Bonnin, Y. Nadot, In situ synchrotron ultrasonic fatigue testing device for 3D characterisation of internal crack initiation and growth, Fatigue Fract. Eng. Mater. Struct. (2019) ffe.13140. https://doi.org/10.1111/ffe.13140.

[21] ASTM E2422-11, Standard Digital Reference Images for Inspection of Aluminum Castings, 2011. www.astm.org.

[22] A. Rotella, Y. Nadot, M. Piellard, R. Augustin, M. Fleuriot, Fatigue limit of a cast Al-Si-Mg alloy (A357-T6) with natural casting shrinkages using ASTM standard X-ray inspection, Int. J. Fatigue. 114 (2018) 177–188. https://doi.org/10.1016/j.ijfatigue.2018.05.026.

[23] R.S. Bellows, S. Muju, T. Nicholas, Validation of the step test method for generating Haigh diagrams for Ti–6Al–4V, Int. J. Fatigue. 21 (1999) 687–697.

[24] D. Lanning, On the use of critical distance theories for the prediction of the high cycle fatigue limit stress in notched Ti-6Al-4V, Int. J. Fatigue. 27 (2005) 45–57. https://doi.org/10.1016/j.ijfatigue.2004.06.002.

[25] W.J. Dixon, A.M. Mood, A Method for Obtaining and Analyzing Sensitivity Data, J. Am. Stat. Assoc. 43 (1948) 109. https://doi.org/10.2307/2280071.

[26] G. Léopold, Y. Nadot, T. Billaudeau, J. Mendez, Influence of artificial and casting defects on fatigue strength of moulded components in Ti-6Al-4V alloy: INFLUENCE OF ARTIFICIAL AND CASTING DEFECTS ON FATIGUE STRENGTH, Fatigue Fract. Eng. Mater. Struct. 38 (2015) 1026–1041.

https://doi.org/10.1111/ffe.12326.

[27] M. Vincent, C. Nadot-Martin, Y. Nadot, A. Dragon, Fatigue from defect under multiaxial loading: Defect Stress Gradient (DSG) approach using ellipsoidal Equivalent Inclusion Method, Int. J. Fatigue. 59 (2014) 176–187. https://doi.org/10.1016/j.ijfatigue.2013.08.027.

[28] C. Geuzaine, J.-F. Remacle, Gmsh: A 3-D finite element mesh generator with built-in pre- and post-processing facilities, Int. J. Numer. Methods Eng. 79 (2009) 1309–1331. https://doi.org/10.1002/nme.2579.

[29] J. Lemaitre, J.-L. Chaboche, A. Benallal, R. Desmorat, Mécanique des matériaux solides - 3ème édition, Dunod, 2009.

[30] Y. Murakami, ed., Effects of Small Defects and Nonmetallic Inclusions, 1. ed, Elsevier, Amsterdam, 2002.

[31] A. Brueckner-Foit, M. Luetje, M. Wicke, I. Bacaicoa, A. Geisert, M. Fehlbier, On the role of internal defects in the fatigue damage process of a cast Al-Si-Cu alloy, Int. J. Fatigue. 116 (2018) 562–571. https://doi.org/10.1016/j.ijfatigue.2018.07.012.

[32] J. Petit, G. Hénaff, Stage II intrinsic fatigue crack propagation, Scr. Metall. Mater. 25 (1991) 2683–2687.